An amplitude equation for surface gravity wave-topography interactions

Jim Thomas and Ray Yamada

Phys. Rev. Fluids **3**, 124802 — Published 13 December 2018

DOI: 10.1103/PhysRevFluids.3.124802

AN AMPLITUDE EQUATION FOR SURFACE GRAVITY WAVE-TOPOGRAPHY INTERACTIONS

JIM THOMAS[†,1,2] AND RAY YAMADA[3]

[1] *Woods Hole Oceanographic Institution, Massachusetts, USA*
[2] *Department of Oceanography, Dalhousie University, Halifax, Canada*
[3] *Department of Earth, Atmospheric and Planetary Sciences, Massachusetts Institute of Technology, Cambridge, Massachusetts, USA*

Abstract. We derive an amplitude equation that captures the effect of small but arbitrary topography on small amplitude surface gravity waves. The robustness of this new reduced model is demonstrated by numerical simulations that compare it with the fully nonlinear water wave equations. The amplitude equation is seen to accurately capture intricate and complex wave dynamics, compared with the fully nonlinear equations, while being much faster than the latter. Consequently, the new model offers great potential for various surface wave-topography interaction investigations, especially when a large number of simulations are needed to obtain wave statistics, a process that is much slower if attempted using the full set of equations.

1. Introduction

Surface gravity waves, primarily generated by atmospheric winds, are ubiquitous in the world's oceans. While in deep water, the ocean floor has a negligible effect on these waves. However, as they travel towards the shore, the topographic features of the seabed play an important role in modulating the waves, resulting in refraction, diffraction, reflection, and scattering of the waves. The surface wave-topography interaction problem is one that has motivated research interests in multiple interdisciplinary scientific communities. Topographic features can invoke resonant interactions between surface waves, popularly known as Bragg resonance, which transfers energy between different waves (Mei, 1983; Craik, 1985; Liu & Yue, 1998). This can result in reflection or deflection of waves away from shores (Heathershaw, 1982; Davies, 1982; Mei, 1985; Yu & Mei, 2000*a*; Couston *et al.*, 2017), which is of interest to coastal engineers as a means to protect shores. Furthermore, wave dynamics play an important role in shaping topographic features such as sand bars and ripples near the coast (Yu & Mei, 2000*b*; Blondeaux, 1990; Hancock *et al.*, 2008), a phenomenon that has intrigued coastal geographers and geomorphologists. From a technological point of view, the abundance of wave energy near the coast makes it a promising source of renewable energy (Evans, 1981; Mei, 2012). However, the wide spread nature of wave energy makes it difficult to extract efficiently. Recently, there has been a growing interest in designing bottom architectures that focus the wave field to enhance wave energy harvesting (Stamnes *et al.*, 1983; Hu & Chan, 2005; Griffiths & Porter, 2012; Elandt *et al.*, 2014).

† jimthomas.edu@gmail.com.

Given the wide range of scientific interests involving wave-topography interactions, mathematical modeling of these interactions have been an active area of research in the past few decades. Modeling surface wave-topography interactions is challenging, since the governing equations are nonlinear and three dimensional with unsteady boundary conditions on the free surface. When faced with problems concerning strongly nonlinear interactions, such as wave steepening at relatively large topography close to the surf zone leading to wave breaking and turbulent mixing (Peregrine, 1983; Battjes, 1988), one must utilize the full equations. However, away from the surf zone, there exists a large variety of scenarios where small amplitude waves interact with small amplitude topography in the form of sand bars, ripples, and coral reefs (see observations reported in Elgar *et al.* 2003; Dolan & Dean 1985; Mandlier 2013; Munk & Traylor 1947 and references therein). In these scenarios, it is highly desirable to have access to simpler mathematical models that faithfully capture the essential features of the interaction. A wide range of reduced models have been proposed for the wave-topography interaction problem. Popular examples include the mild slope equation, which assumes a small slope for the bottom topography, and its various improvements (Berkhoff, 1973; Kirby, 1986; Chamberlain & Porter, 1995; Miles & Chamberlain, 1998), ordinary differential equations for the interaction of a few plane waves with simple sinusoidal seabeds (Mei, 1985; Couston *et al.*, 2017), and ray tracing or geometric optics applied to surface waves propagating over a slowly varying topography, assuming a spatial scale separation between the wave field and topography (Munk & Traylor, 1947; Keller, 1958).

In spite of the variety of simple models derived in the past, amplitude equation models remain completely unexplored for this problem. Amplitude equations are simple models with multiple benefits over the reduced models discussed before, which include filtering out fast oscillations allowing for larger time steps during numerical integration and not requiring spatial scale separation between the wave and interacting field. For problems involving waves, amplitude models are extremely useful in a variety of scenarios corresponding to wave-wave, wave-mean flow and wave-medium interactions. While much work has addressed nonlinear surface wave-wave interactions with amplitude equations (see for example Craik 1985; Ablowitz 2011 and references therein), we are unaware of any previous work that has attempted to derive an amplitude equation aimed at capturing the effect of an arbitrary topography on surface waves. This sets the primary motivation for the present work. We derive an amplitude equation that captures the evolution of a monochromatic (single frequency) wave field interacting with a small amplitude but spatially arbitrary (i.e. spatially broadband) topography. Notably, we do not assume any spatial scale separation between the wave field and the topography, which makes the model ideal for capturing class I Bragg resonant interactions. We establish the robustness of the new model by numerically comparing it with the fully nonlinear surface wave equations. Given the simplicity of the new model and its capability to capture extreme wave-topography interactions as demonstrated by our numerical simulations, we believe the amplitude equation will have a wide range of applications in the future, especially in the ocean engineering community where fast and efficient numerical integration of the governing equations is a priority.

The plan for this paper is as follows: we derive and discuss the new amplitude equation in §2, present a series of numerical experiments that test the model against the fully nonlinear equations in §3 and summarize our findings in §4.

2. A new amplitude equation

The full three dimensional nonlinear equations governing the dynamics of irrotational water waves encountering an arbitrary topography are:

$$\Delta\phi + \partial^2\phi/\partial z^2 = 0 \tag{1a}$$

$$z = \eta(\boldsymbol{x}, t): \ \partial\phi/\partial t + g\eta + \frac{1}{2}\left[(\nabla\phi)^2 + (\partial\phi/\partial z)^2\right] = 0, \tag{1b}$$

$$\partial\eta/\partial t - \partial\phi/\partial z + \nabla\phi\cdot\nabla\eta = 0 \tag{1c}$$

$$z = -H + \zeta(\boldsymbol{x}): \ \partial\phi/\partial z = \nabla\zeta\cdot\nabla\phi \tag{1d}$$

where η and ζ denote the time evolving free surface displacement and the stationary-in-time bottom topography with respect to the fluid level at $z = 0$ and $z = -H$, respectively. The fluid exhibiting potential flow in the region $-H+\zeta \le z \le \eta$ with no vorticity is expressed by (1a), ϕ being the three dimensional potential whose gradient gives the velocity field. From Bernoulli's equation we get the dynamic condition (1b) that ensures continuity of pressure across the free surface, (1c) expresses the condition that the top free surface remains a material surface, and (1d) imposes that the velocity normal to the bottom boundary must vanish, since the bottom topography is impenetrable. Finally, g is the acceleration due to gravity, $\boldsymbol{x} = (x, y)$, $\nabla = (\partial/\partial x, \partial/\partial y)$ and $\Delta = \partial^2/\partial x^2 + \partial^2/\partial y^2$.

We assume small amplitude waves, i.e. $a \ll 1$, where a denotes the wave amplitude. Consequently, we drop the nonlinear terms that arise in (1b) and (1c). We further assume asymptotically small bottom topography, i.e. $\zeta/H \sim O(\epsilon) \ll 1$, where ϵ is the small parameter in the problem. Thus we obtain the linearized interaction equations:

$$\Delta\phi + \partial^2\phi/\partial z^2 = 0 \tag{2a}$$

$$z = 0: \ \partial\phi/\partial t + g\eta = 0, \ \partial\eta/\partial t - \partial\phi/\partial z = 0 \tag{2b}$$

$$z = -H: \ \partial\phi/\partial z = \epsilon\nabla\cdot(\zeta\nabla\phi) \tag{2c}$$

where (2b) and (2c) follows from the Taylor series expansion of (1b), (1c) and (1d) with respect to $z = 0$ and $z = -H$. Noting that g and H are two parameters that appear in the above equations, we can use them to construct length, velocity, and time scales H, $\sqrt{gH}$ and $\sqrt{H/g}$. Hereafter we shall treat (2) as the system obtained after nondimensionalizng with these scales. In this sense, $g = H = 1$, although we retain them in the equations throughout for clarity. Concomitantly, ζ is $O(1)$ henceforth, with ϵ in (2c) indicating the smallness of the topography. Note that the approximations we used above to obtain (2) sets us in the regime of small amplitude waves interacting with asymptotically small bottom topography with the appropriate scaling $a \ll \epsilon \ll 1$.

In the absence of topography, i.e. in the limit $\epsilon = 0$, (2) admits exact plane wave solutions of the form

$$\phi(\boldsymbol{x}, z, t) = \frac{\cosh(k_0(z+H))}{\cosh(k_0 H)} e^{i(\boldsymbol{k}_0\cdot\boldsymbol{x} - \omega_0 t)} + \text{c.c.} \tag{3a}$$

$$\text{where } \omega_0 = \sqrt{g k_0 \tanh(k_0 H)} \tag{3b}$$

and c.c. denotes complex conjugate. Observe that the wave frequency ω_0 depends only on the magnitude of the wavenumber vector, $k_0 = |\boldsymbol{k}_0|$, and not on its orientation, and similarly for the vertical structure in (3a). We use (3a) as the basis for our asymptotic solution, which holds to a good approximation for small but non zero topography ($\epsilon \ll 1$). The topography catalyzes class I Bragg resonant interactions which result in energy transfer from an incident wave to wave modes of the same frequency, spatial scale, and vertical structure, but with varying horizontal

directions. Consequently, the general solution will involve a collection of wave modes with different wavenumbers and may be represented by a generalization of (3a) as

$$\phi(\boldsymbol{x}, z, t, T) = e^{-i\omega_0 t}\frac{\cosh(k_0(z+H))}{\cosh(k_0 H)}A(\boldsymbol{x}, T) + \text{c.c.} \tag{4}$$

Here A represents the wave amplitude, containing the horizontal structure of the wave field, and is expected to evolve on a slow time scale $T = \epsilon t$ due to the smallness of the topography. Below we derive an evolution equation for the wave amplitude.

2.1. **Derivation of the amplitude equation.** Although surface wave evolution is governed by three dimensional equations, wave propagation is constrained to the horizontal plane, i.e. these waves do not exhibit propagation in the vertical direction. The first step in deriving an amplitude equation for a monochromatic wave field is separating the propagating horizontal part from the full three-dimensional field by vertical averaging. We use Green's identity to accomplish this, along the same lines as Smith & Sprinks (1975) and Kirby (1986). Setting $\phi = f(z)\psi(\boldsymbol{x}, t)$ with $f(z) = \cosh(k_0(z+H))/\cosh(k_0 H)$ and applying Green's second identity to the functions f and ϕ gives:

$$\int_{-H}^{0} (\phi f_{zz} - f\phi_{zz})\, dz = [\phi f_z - f\phi_z]_{-H}^{0} \tag{5}$$

Using (2) in (5), we get:

$$\int_{-H}^{0} \left[f_{zz} f(z)\psi + (\Delta\psi) f^2(z)\right] dz = f(0)k_0 \tanh(k_0 H)\psi + \frac{f^2(0)}{g}\frac{\partial^2\psi}{\partial t^2} + \epsilon f^2(-H)\nabla\cdot(\zeta\nabla\psi) \tag{6}$$

We simplify further using

$$\int_{-H}^{0} f^2(z) dz = \frac{1}{2}\left(H\,\mathrm{sech}^2(k_0 H) + \frac{\tanh(k_0 H)}{k_0}\right) = \frac{cc_g}{g} \tag{7}$$

where $c = \omega_0/k_0$ and $c_g = \omega_0'(k_0)$ represent the phase and group velocities respectively. Thus we get an evolution equation for ψ:

$$\frac{\partial^2\psi}{\partial t^2} + \omega_0^2\psi - cc_g\left(\Delta\psi + k_0^2\psi\right) + \frac{\epsilon g}{\cosh^2(k_0 H)}\nabla\cdot(\zeta\nabla\psi) = 0 \tag{8}$$

Equation (8) is a reduction of (2) that isolates the propagating part of the wave field by removing the vertical dependence. We note that time step required for numerically integrating the linear equations, (8) and (2), is set by the need to capture fast oscillations of the wave with time period $2\pi/\omega_0$. However, the topographic interaction term is $O(\epsilon)$ and therefore would modify the wave field by an $O(1)$ amount on an $O(1/\epsilon)$ timescale. Consequently, straightforward numerical integration of the equations to capture significant changes in the wave field induced by the topography would require integrating up to time scales of $O(1/\epsilon)$ with small enough time steps to resolve the fast oscillations, with time period $2\pi/\omega_0$. We overcome this issue of requiring small time steps to capture fast oscillations by implementing the method of multi-time-scale asymptotics to derive an amplitude equation that filters the fast oscillatory part of the wave field, thus allowing the usage of asymptotically larger time steps to track the effect of bottom topography on the waves. For this

purpose, we introduce a slow time scale $T = \epsilon t$ and redefine time derivative as $\partial/\partial t \to \partial/\partial t + \epsilon\partial/\partial T$ to rewrite the above equation as

$$\frac{\partial^2\psi}{\partial t^2} + \omega_0^2\psi - cc_g\left(\Delta\psi + k_0^2\psi\right) + \epsilon\left(2\frac{\partial^2\psi}{\partial t\partial T} + \frac{g}{\cosh^2(k_0H)}\nabla\cdot(\zeta\nabla\psi)\right) + \epsilon^2\frac{\partial^2\psi}{\partial T^2} = 0 \tag{9}$$

We then expand ψ asymptotically as $\psi = \psi_0 + \epsilon\psi_1 + O(\epsilon^2)$. At leading order we get:

$$\frac{\partial^2\psi_0}{\partial t^2} + \omega_0^2\psi_0 - cc_g\left(\Delta\psi_0 + k_0^2\psi_0\right) = 0 \tag{10}$$

We write the solution of above equation as

$$\psi_0 = A_0(\boldsymbol{x}, T)e^{-i\omega_0 t} + \text{c.c.} \tag{11}$$

which gives us

$$-cc_g\left(\Delta A_0 + k_0^2 A_0\right) = 0 \tag{12}$$

Notice that unlike usual asymptotic approaches (see for example Hinch 1991), we do not write down an exact solution to the leading order equation (10). Instead, we let the amplitude A_0 posses an arbitrary spatial structure, consistent with (12), which means that the spectrum of A_0 can potentially contain several Fourier modes with wavenumbers of the same magnitude, so as to have the same frequency, ω_0. Any such collection of Fourier modes with the same wavenumber magnitude will exactly satisfy (12). Our goal is to derive an amplitude equation that can track the evolution of a collection of such Fourier modes. We therefore do not impose a pre-determined spatial structure on A_0, but rather let it evolve based on the effect of topography on the wave field. This will be accomplished by the inclusion of the topographic interaction term at the next order of asymptotics. To derive an evolution equation for the wave amplitude, we modify (12) by setting

$$-cc_g\left(\Delta A_0 + k_0^2 A_0\right) = \epsilon\Gamma \tag{13}$$

where Γ is an $O(1)$ quantity and will be evaluated at the next order of asymptotics. Such an approach, of combining the leading order and next order terms to form a single equation, is known as reconstitution (Roberts, 1985) and has been successfully used for several asymptotic problems in recent times – see for example Wagner & Young (2016), Thomas (2017), Wagner *et al.* (2017), Thomas *et al.* (2017), and Thomas (2016). The same technique was used by Dysthe (1979) and Trulsen & Dysthe (1996) for surface wave problems (also see Ablowitz 2011 for several other applications of this technique).

Continuing the asymptotic expansion, at $O(\epsilon)$ of (9) we get:

$$\frac{\partial^2\psi_1}{\partial t^2} + \omega_0^2\psi_1 - cc_g\left(\Delta\psi_1 + k_0^2\psi_1\right) + \left(\Gamma e^{-i\omega_0 t} + \text{c.c.}\right) + \left(2\frac{\partial^2\psi_0}{\partial t\partial T} + \frac{g}{\cosh^2(k_0H)}\nabla\cdot(\zeta\nabla\psi_0)\right) = 0 \tag{14}$$

At this order we set

$$\psi_1 = A_1(\boldsymbol{x}, T)e^{-i\omega_0 t} + \text{c.c.} + \text{NRT} \tag{15}$$

where NRT above indicate non-resonant terms, since they have frequency different from ω_0, but necessarily contribute to the complete solution at $O(\epsilon)$. We substitute above expression for ψ_1 in (14), collect terms multiplied by $e^{-i\omega_0 t}$ and set them to zero, this being the solvability condition for ensuring the absence of secular growth in the solution (see for example Ablowitz 2011), to obtain

$$\Gamma - cc_g\left(\Delta A_1 + k_0^2 A_1\right) + \left(-2i\omega_0\frac{\partial A_0}{\partial T} + \frac{g}{\cosh^2(k_0H)}\nabla\cdot(\zeta\nabla A_0)\right) = 0 \tag{16}$$

Notice that in (16) we have an expression for Γ. We use this expression for Γ in (13), define $A = A_0 + \epsilon A_1$, ignore $O(\epsilon^2)$ terms and rearrange terms to get

$$\frac{\partial A}{\partial T} - i\frac{cc_g}{2\epsilon\omega_0}\left(\Delta A + k_0^2 A\right) + i\frac{g}{2\omega_0\cosh^2(k_0 H)}\nabla\cdot(\zeta\nabla A) = 0 \tag{17}$$

The above equation is an amplitude equation for the evolution of the leading order wave field, where the fast oscillatory part, $e^{-i\omega_0 t}$ has been removed, allowing us to focus better on the topographic interaction via the final term. We conclude our derivation with one final step, proceeding along the same lines as Wagner & Young (2016), Thomas (2017), and Wagner *et al.* (2017), that will improve the dispersive characteristics of (17).

The surface wave dispersion relationship, $\omega(k) = \sqrt{gk\tanh(kH)}$, can be expanded in a Taylor series about $(k_0, \omega(k_0))$ to obtain:

$$\omega(k) = \omega(k_0) + (k-k_0)\omega'(k_0) + (k-k_0)^2\omega''(k_0) + ... \tag{18}$$

On the other hand, the reduced dispersion relationship of the amplitude equation is obtained by using a plane wave solution of the form $A = \tilde{A}e^{i(\boldsymbol{k}\cdot x - \Omega T)}$ in (17). This procedure gives us:

$$\Omega(k) = \left(\frac{cc_g}{2\epsilon\omega_0}\right)\left(k^2 - k_0^2\right) \tag{19}$$

We observe that $\Omega(k_0) = 0$ since $\Omega(k)$ captures the deviation from the leading frequency $\omega_0 = \omega(k_0)$, as a consequence of fast phase removal in (11) and (15). Furthermore, we have $\Omega'(k_0) = c_g/\epsilon = \omega'(k_0)/\epsilon$ (note that the appearance of ϵ is due to the usage of 'slow time', T). However, we find that $\Omega''(k_0) = cc_g/\epsilon\omega_0 \neq \omega_0''(k_0)/\epsilon$. This means that the reduced model (17) can approximate the series expansion of full dispersion relationship given in (18) only up to $O(k-k_0)$, failing to capture $O((k-k_0)^2)$ effects. We overcome this limitation of amplitude equation to obtain an improved model capable of capturing second order wavenumber effects in the dispersion relationship.

Time differentiating (13), after setting $A_0 = A + O(\epsilon)$, we get $\partial/\partial T\left(\Delta A + k_0^2 A\right) = O(\epsilon)$. We multiply this with a yet-to-be-determined variable α and add this to (17), ignoring the topographic interaction term temporarily, to get

$$\frac{\partial}{\partial T}\left(A + \alpha(\Delta + k_0^2)A\right) - i\frac{cc_g}{2\epsilon\omega_0}\left(\Delta A + k_0^2 A\right) = 0 \tag{20}$$

Substituting a plane wave solution to the above equation in the form $A = \tilde{A}e^{i(\boldsymbol{k}\cdot x - \Omega T)}$ gives us the dispersion relationship

$$\Omega(k) = \left(\frac{cc_g}{2\epsilon\omega_0}\right)\frac{k^2 - k_0^2}{1 + \alpha\left(k_0^2 - k^2\right)} \tag{21a}$$

$$\Rightarrow \Omega'(k_0) = \frac{c_g}{\epsilon} \text{ and } \Omega''(k_0) = \frac{c_g}{\epsilon}\left[\frac{c}{\omega_0} + 4\alpha k_0\right] \tag{21b}$$

Note that we recover (19) from (21a) in the limit $\alpha = 0$. To improve the dispersive features of the amplitude equation up to $O((k-k_0)^2)$, we set $\Omega''(k_0) = \omega_0''(k_0)/\epsilon$. This gives us a unique value for α: $\alpha = (k_0\omega''(k_0) - \omega'(k_0)/(4k_0^2\omega'(k_0))$, using which we get the improved amplitude equation:

$$\left[1 + \alpha(\Delta + k_0^2)\right]\frac{\partial A}{\partial T} - i\beta\left(\Delta + k_0^2\right)A + i\gamma\nabla\cdot(\zeta\nabla A) = 0 \tag{22}$$

$$\text{where } \alpha = \frac{1}{4k_0^2\omega'(k_0)}\left(k_0\omega''(k_0) - \omega'(k_0)\right),\ \beta = \frac{\omega_0'(k_0)}{2k_0\epsilon},\ \text{and } \gamma = \frac{g}{2\omega_0(k_0)\cosh^2(k_0 H)}$$

whose dispersive characteristics are better than that of (17), since it approximates the full dispersion relationship in (18) up to $O((k-k_0)^2)$. We tested the improvement of (22) over (17) with a wide

range of numerical simulations, corresponding to those discussed in §3, comparing both amplitude equations against the full set of equations (1) and the linear equations (2) and (8). The modified equation (22) was seen to perform consistently better than (17) (see appendix B for an example), these results being similar to those shown in figures 6 and 10 in Thomas (2017).

2.2. **Features of the amplitude equation.** We now examine some of the features of the new amplitude equation model, (22). Observe that the final term is the topographic interaction term, which by triadic interaction with pre-existing wave modes would generate new wavenumbers in the spectrum of A, thus changing its spatial structure. A simple reduction of the amplitude equation is achieved for the case of two plane waves interacting with a sinusoidal topography. Consider two plane waves given by $A = A_1 e^{i\boldsymbol{k}_1\cdot\boldsymbol{x}} + A_2 e^{i\boldsymbol{k}_2\cdot\boldsymbol{x}}$ (the plane wave form for the potential is obtained by substituting this in (4)) with $k_1 = k_2 = k_0$, so that they possess the same frequency, $\omega_0(k_0)$, propagating over a simple topography of the form $\zeta = \zeta_0 e^{i\boldsymbol{k}_b\cdot\boldsymbol{x}} + \text{c.c.}$, where ζ_0 is the constant amplitude of the topography with wavenumber $\boldsymbol{k}_b$ such that $\boldsymbol{k}_2 = \boldsymbol{k}_1 + \boldsymbol{k}_b$. Truncating (22) to the above two wave modes, noting that for this special case of resonant modes the term $(\Delta + k_0^2)A$ identically vanishes, we get the equations:

$$\frac{dA_1}{dT} - i\gamma\left(\boldsymbol{k}_1\cdot\boldsymbol{k}_2\right)\zeta_0^* A_2 = 0,\ \frac{dA_2}{dT} - i\gamma\left(\boldsymbol{k}_1\cdot\boldsymbol{k}_2\right)\zeta_0 A_1 = 0 \tag{23}$$

The reduced model (23) illustrates how topography can passively induce energy transfer between two plane waves with amplitudes A_1 and A_2. The exact analytical solution of the above equations can be written down, the solutions being time-periodic oscillations with a period that depends on the value of ζ_0. The interaction is energy preserving, i.e. $|A_1|^2 + |A_2|^2$ is a constant independent of time, as can be easily shown using (23).

A further special simplification of the reduced mode (23) is obtained by setting $\boldsymbol{k}_2 = (k, 0)$, $\boldsymbol{k}_b = (2k, 0)$ and $\boldsymbol{k}_1 = (-k, 0)$. In this example, a left going wave with wavenumber $\boldsymbol{k}_1$ is reflected by topography with half the wavelength by generating a counter-propagating wave $\boldsymbol{k}_2$, which demonstrates wave reflection by bars or ripples on beaches (Mei, 1985; Couston *et al.*, 2017). Note that an arbitrary spatially broadband topography consists of many Fourier modes and cannot be represented by a single Fourier mode as above. Consequently, considering the exact triadic resonant modes alone would yield an extremely large number of equations similar to (23). This fundamental difficulty is probably why an amplitude equation was not derived for this problem in the past. We used the technique of combining reconstitution with multi-time-scale asymptotics to obtain an amplitude equation, (22), in physical space, which essentially contains an assemblage of all possible exact resonant equations of the form (23) in spectral space.

In addition to exactly resonant modes, i.e. Fourier modes that satisfy $|\boldsymbol{k}| = k_0$ with frequency ω_0, the amplitude equation (22) also captures the dynamics of near-resonant modes. A certain Fourier mode $\boldsymbol{k}$ is near-resonant if $|\boldsymbol{k}| = k_0 + \delta$, where δ is asymptotically small but non-zero. Consequently, these near-resonant modes have frequencies slightly off the exact value of ω_0 by an amount $O(\delta)$. While the term $\left(\Delta + k_0^2\right) A$, (note that although this term appears twice in the amplitude equation, here and below we are referring to the term multiplied by β, and not the term associated with the time derivative) vanishes for exact resonant modes, this term is non-zero for near-resonant modes, the magnitude being $O(\delta)$, i.e. the amount by which the modes are off-resonant. Therefore, while resonant modes will be strongly modified by topography as a result of the exact vanishing of the term $\left(\Delta + k_0^2\right) A$ for these modes, near-resonant modes will be modulated to a lesser extent, the strength of modulation being proportional to the smallness of δ. Finally, we note that the triadic interaction term involving topography in the amplitude equation also generates non-resonant modes,

i.e. modes $\boldsymbol{k}$ that satisfy $|\boldsymbol{k}| - k_0 \sim O(1)$, for which $\left(\Delta + k_0^2\right) A$ is $O(1)$. These modes will undergo almost no modulation, in comparison to resonant and near-resonant modes.

We therefore observe that although resonant, near-resonant, and non-resonant modes are generated by the topographic triadic interaction term in the amplitude equation, the $\left(\Delta + k_0^2\right) A$ term acts as a 'selective filter' by vanishing exactly and nearly so for resonant and near-resonant modes and thus promoting strong modulation of these modes, while blocking non-resonant modes and thereby preventing their modulation. Strong modulation of resonant and near-resonant modes due to the term $\left(\Delta + k_0^2\right) A$ being zero or nearly zero means that the amplitude equation can be integrated with larger time steps, compared to (2) or (8), while accurately capturing the evolution of resonant and near-resonant modes – a strategy is to treat this term implicitly in numerical integrators. For various simulations, corresponding to those discussed in §3, we found that the amplitude equation could be integrated with time steps roughly $1/\epsilon$ larger than that used to integrate (2) or (8). For example, when $\epsilon = 0.1$ a value we chose for numerical experiments presented in §3, we were able to integrate the amplitude equation with time steps almost 10 times larger than that used for integrating (2) or (8). The newly derived amplitude equation (22) therefore serves as an optimal single equation model, particularly set in physical space (and not in spectral space), that can be integrated faster and conveniently while collectively tracking resonant and near-resonant wave modes.

We conclude this section by noting conservation laws associated with (22). As discussed in Thomas (2017), by multiplying the amplitude equation by A^* and iA_T^*, and integrating over the whole domain, D, assuming vanishing boundary fluxes (for example due to periodic or unbounded domains) and taking the real part of the result, we get the following two conservation laws:

$$\frac{d}{dT}\int_D \left[\left(1 + \alpha k_0^2\right)|A|^2 - \alpha|\nabla A|^2\right] d\boldsymbol{x} = 0 \tag{24a}$$

$$\frac{d}{dT}\int_D \left[\beta\left(k_0^2|A|^2 - |\nabla A|^2\right) + \gamma\zeta|\nabla A|^2\right] d\boldsymbol{x} = 0 \tag{24b}$$

These conservation laws are valuable tools in testing validity of numerical integration schemes used for (22). For the simulations discussed in §3, we checked that above conservation laws were satisfied by the numerical scheme up to a high degree of accuracy.

3. Two applications of the amplitude equation

We now examine the accuracy of the amplitude equation (22), by comparing it with the full three dimensional nonlinear equations (1) with a series of numerical simulations. The purpose of our comparison of the amplitude equation with the full nonlinear set of equations is to demonstrate that the amplitude equation, derived with the usage of asymptotics, is able to capture features that the full set of equations would exhibit in the asymptotic regime, a point that is not obvious without numerical experiments comparing the two models. Furthermore, our simulations were conducted using physical setups which involve complex topographies that give rise to non trivial surface wave phenomena via wave-bottom interactions. Several previous investigators have conducted these experiments with the full set of equations due to their complexity, but here we show that the new model (22) can accurately and efficiently capture these phenomena.

Numerical integration of (22) and (1) used pseudospectral codes with RK4 for time integration. High-order spectral method (Dommermuth & Yue, 1987, West *et al.*, 1987, HOSM hereafter) was used to integrate (1). HOSM is implemented by applying a converging Taylor series expansion to the governing equations, (1), up to an arbitrary order of nonlinearity, M. HOSM is a very

robust scheme with exponential convergence achievable for problems where the wave steepness and bottom topography is small, and has been successfully used for various wave-topography interaction problems (Liu & Yue, 1998, Alam *et al.*, 2009, Alam *et al.*, 2010). In this regard, HOSM is a state-of-the-art technique to integrate (1), particularly since we are operating in the regime of asymptotically small wave amplitudes and bottom topography. The results reported here are based on simulations with a spatial resolution of $N = 512$. Numerical convergence was ensured by decreasing time steps and increasing spatial resolution so that only a small fraction of domain integrated total wave energy was lost during the whole simulation. Although we found that the nonlinear solutions were well captured by HOSM with $M = 3$, all the experiments in this section were conducted with $M = 4$ for higher accuracy. To compare η obtained by integrating the full set of equations in (1) with the amplitude equation (22), the amplitude field, A, was used in (4) and (2b) to obtain the asymptotic surface displacement field, η, as $\eta = i(\omega_0/g)A + \text{c.c.}$.

All of our simulations were initialized with a single plane wave with $\boldsymbol{k} = (1, 0)$ corresponding to a wavelength $\lambda = 2\pi$ in a doubly periodic square domain of length 40λ and mean vertical depth $H = 1$ (therefore $kH = 1$). We chose the topographic features to have spatial scales comparable to λ, thus preventing any spatial scale separation between wave and topography fields. The height of the topography is set by ϵ, and we chose different values for ϵ ranging from 0.1 to 0.35. We choose a wave amplitude $a = 0.01$, so that even for our smallest value of ϵ, 0.1, the wave amplitude was asymptotically small in comparison, ensuring that modulation of the solution by nonlinear wave interactions was minimal, consistent with our initial assumption of small amplitude waves leading to (2).

3.1. **Surface wave scattering.** The first experimental set up was designed to capture arbitrary scattering of an incident plane wave by random bottom topography. We generated the random topography ζ for our simulation using a homogeneous isotropic Gaussian random field with correlation length λ. The topography was doubly periodic spanning the whole domain and was scaled to have a maximum amplitude of ϵ when integrating (1), but when integrating (22) we divided ζ by ϵ so that it is $O(1)$. The correlation length was chosen so that the topographic and wave fields are of the same spatial scale to facilitate maximum attainable interaction within this set up.

Figure 1(a) shows the surface wave scattering that emerged after 100 wave periods for $\epsilon = 0.15$. The random topography is shown underneath the surface wave field in the schematic (a detailed figure of the topographic field ζ is included in appendix A and a movie showing the development of the wave scattering is included in the supplementary materials). Although the wave field is initially a single plane wave with $k_x = 1$ and $k_y = 0$, the topography promotes energy transfer between various modes, as discussed above in §2.2, thus generating many new wavenumbers. Consequently, the free surface displacement η develops irregular and elongated wave envelopes highlighted in red. Figure 1(b) shows the scaled magnitude of the same surface wave field ($|\eta|/a$) but zoomed in over a subdomain. The crests and troughs from the initial plane wave can be clearly seen inside the larger wave envelopes. The scattering of energy to different modes becomes more apparent when looking at the spectrum of η. Figure 1(c) shows the quantity $|\hat{\eta}(\boldsymbol{k})|$ computed from the amplitude model, where $\hat{\eta}(\boldsymbol{k})$ denotes the Fourier transform of η. At $t = 0$, due to the single plane wave initialization, all of the energy is concentrated at just two points: $\boldsymbol{k} = (\pm 1, 0)$. However, with increasing time, the wave energy gets transferred to various modes on and around the $k = 1$ circle in spectral space, corresponding to resonant and near-resonant modes. Figures 1(d) and 1(e) show the corresponding plots to 1(b) and 1(c) computed from the full nonlinear equations, showing an excellent pointwise agreement with the amplitude equation.

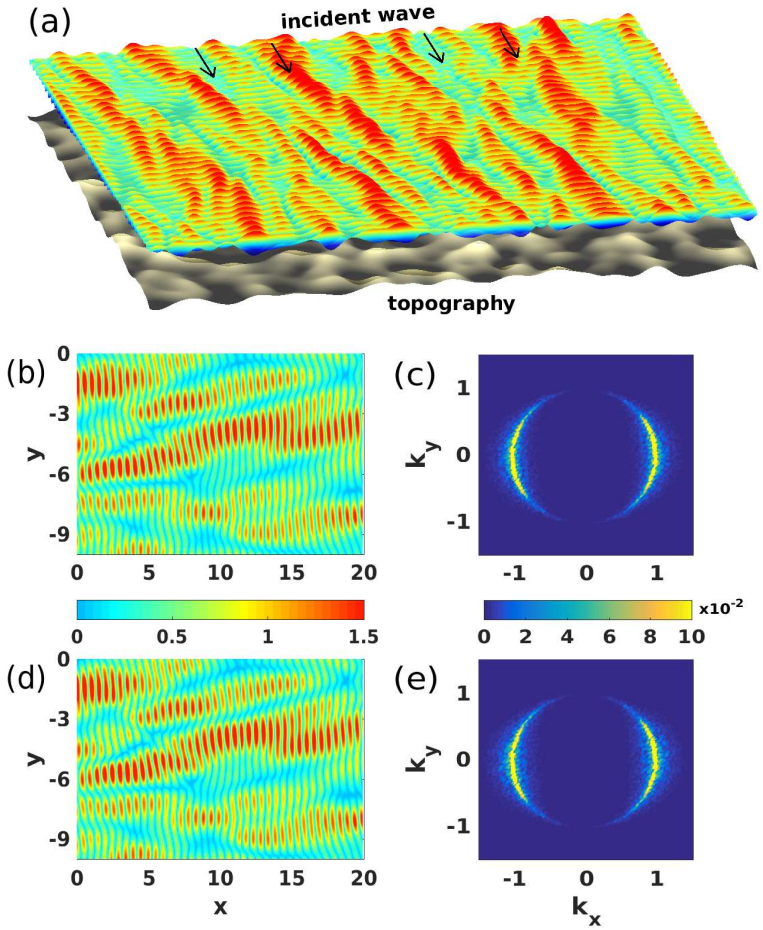

FIGURE 1. (a) Three-dimensional depiction of surface gravity wave scattering, showing the free surface displacement η computed from the amplitude equation (22) at the final time of integration $t = 720$ (100 wave periods) and the random topography underneath for $\epsilon = 0.15$. Incident waves enter the domain from the far side and are scattered by the bottom topography, as can be seen by the irregular and elongated wave envelopes (features highlighted in red) which have developed. Panels (b) and (c) show the scaled magnitude of the surface wave field, $|\eta|/a$, and the Fourier spectrum of η at the same time, obtained by integrating the amplitude equation. Panels (d) and (e) are the same quantities shown in (b) and (c), but obtained by integrating the fully nonlinear equations (1).

3.2. **Surface wave focusing.** In contrast to the previous experiment where a random topographic field scatters and inhomogenizes an organized wave field, we now consider a physical set up consisting of specially designed topography to focus waves onto a certain region. This experimental set up was inspired by questions regarding the efficient placement of wave energy conversion devices along coasts in an attempt to harvest renewable energy from waves (Mei, 2012). Since surface waves are spread out across large areas, localizing the wave energy through focusing can improve the efficiency of wave energy extraction, by having fewer wave energy conversion devices in designated locations. From an engineering point of view, the challenge is the optimal design of topography to achieve wave focusing, which crucially depends on numerically integrating the wave-topography interaction equations. The fast integration achieved by the amplitude equation allows one to easily assess a large collection of designs in search for an optimal solution.

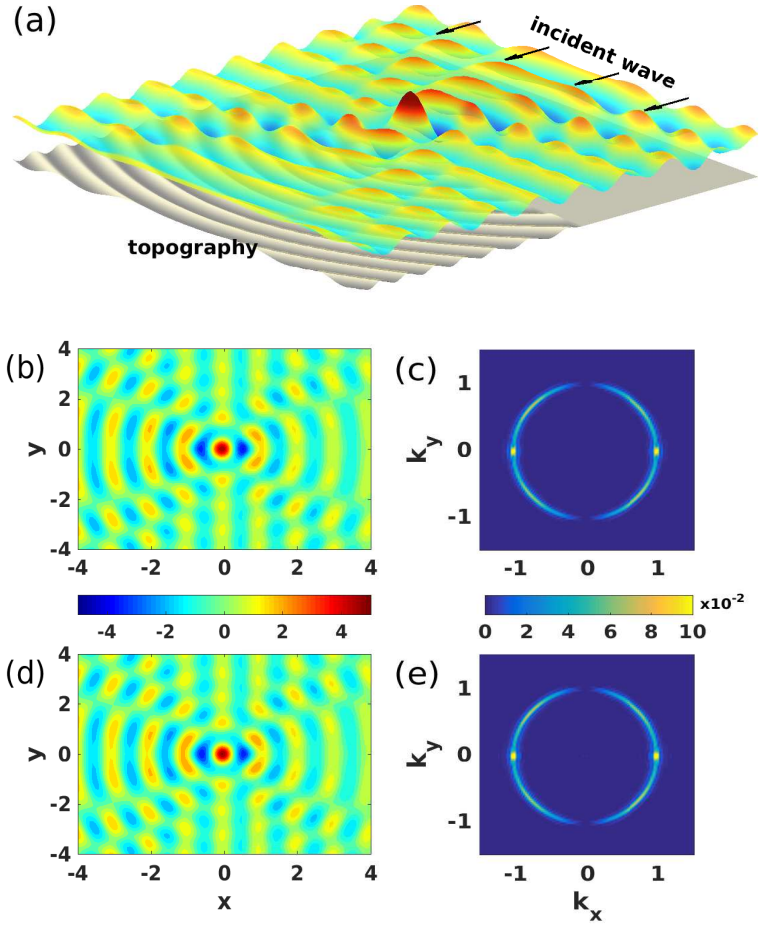

FIGURE 2. (a) Three-dimensional depiction of surface gravity wave focusing, showing the free surface displacement η computed from the amplitude equation (22) at $t = 152$ (21.2 wave periods), a time of maximum focusing after equilibration is reached with a focal amplitude of $5.0a$. The topography ζ is shown underneath and is shaped as a concave mirror designed to focus the incident waves (entering from the right side) at the center of the domain. The focal point is indicated by the red peak at the center. Panels (b) and (c) show the amplification η/a and the spectrum of η, while (d) and (e) are the same quantities obtained by integrating the fully nonlinear equations (1).

We designed a topographic structure to achieve wave focusing following the theoretical and experimental set up discussed in Elandt *et al.* (2014) – see appendix A for the exact equations that were used to construct the topography. The topography thus constructed occupies $1/16^{\text{th}}$ of the domain and acts as a "concave mirror" that redirects incident wave energy towards a focal point at the origin. Figure 2(a) illustrates the setup of the simulation for the case $\epsilon = 0.15$, showing a zoomed-in region near the focal point. Starting from an initial plane wave of amplitude a, the wave crests that pass through the focal point grow in height until reaching a maximum amplitude of $5a$, which was seen to be maintained after 15 wave periods. A movie illustrating the wave development can be found in the supplementary materials.

Figures 2(b)-(e) compare the surface wave field η computed from the amplitude equation (top row) and full nonlinear equations (bottom row) in both physical and spectral space. As in the case of

scattering, there is an excellent agreement between the two equations for focusing. The spectrum shows that the modes that lie on and around the ring $k = 1$ become excited, having had all the initial energy concentrated at $\boldsymbol{k} = (\pm 1, 0)$.

3.3. **Quantifying model performance.** We now turn our attention to quantify the differences between the amplitude equation and the fully nonlinear equations for the two physical setups discussed before. A stringent metric to compare the two models is computed by the pointwise difference between the wave fields generated by the models. For this, we define the normalized root-mean-square error as

$$\mathcal{E}_{\text{rms}} = \left(\int_B (\eta_{\text{amp}} - \eta_{\text{NL}})^2 \, d\boldsymbol{x} \Big/ \int_B \eta_{\text{NL}}^2 \, d\boldsymbol{x} \right)^{1/2} \tag{25}$$

where η_{amp} and η_{NL} denote η for the amplitude and the fully nonlinear equations, respectively, and B is the region of interest over which the difference is computed. For the scattering experiment, B is the entire spatial domain, while in the focusing experiments, B is a disk centered at the focal point with radius 4λ.

Figure 3(a) shows $\mathcal{E}_{\text{rms}}$ computed for the scattering (blue) and focusing (red) experiments discussed in figures 1 and 2 as a function of time. For both of these experiments, we note that the error remains $O(\epsilon)$, ϵ being 0.15 for these experiments. This is the order of error we expect based on the technique of multi-scale-asymptotics used to derive the amplitude equation. Recall that the topographic interaction term in (2) is $O(\epsilon)$ and therefore negligible for a few wave periods. However, on $1/\epsilon$ timescale, corresponding to $T \sim O(1)$, this weak term is capable of changing the wave field by an $O(1)$ amount. By using the method of multi-time-scale asymptotics, we ensure that the amplitude equation captures the $O(1)$ dynamics of the wave field up to $O(1/\epsilon)$ timescales, and therefore succeeds in maintaining the error between the asymptotic model and the fully nonlinear model to an $O(\epsilon)$ amount. However, we emphasize here that the error remains $O(\epsilon)$ even in the presence of nonlinear terms that arise in (1) and on integrating for a much longer time than the asymptotic estimate of a $1/\epsilon$ timescale (observe especially the scattering experiment, which was conducted for 100 wave periods), results that strengthen the validity of the amplitude equation.

To test the robustness of the amplitude equation, we used a series of scattering and focusing experiments with all parameters the same as before except for ϵ which was varied from 0.1 to 0.35. The scattering experiments were run to the same slow time $T = 100$ (or $t = 100/\epsilon$). The focusing experiments were run to 30 wave periods for the different values of ϵ because after around 15 wave periods the focal maximum did not change and the simulations reached a quasi steady state with negligible changes in $\mathcal{E}_{\text{rms}}$. We therefore ran focusing experiments up to 30 wave periods for all values of ϵ.

Figure 3(b) shows $\mathcal{E}_{\text{rms}}$ versus ϵ for the set of scattering (blue, dots) and focusing (red, squares) experiments. As expected, based on above discussion of error being $O(\epsilon)$, increasing ϵ is seen to increase the error. From figure 3(b) we conclude that based on the strict metric of pointwise error, values of ϵ around 0.15 is optimal, for error to remain below 20%. However, we note that pointwise error metrics are very stringent, and often one is interested in efficient and fast calculation of various wave statistics. We therefore ask – how large can ϵ be for wave statistics obtained from the two models to agree within a reasonable degree? We attempt to answer this question by examining two statistical quantities corresponding to the experiments described before.

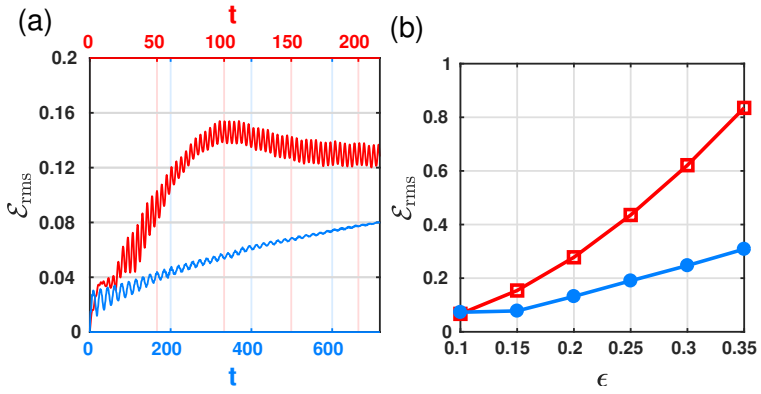

FIGURE 3. (a) The root-mean-square error $\mathcal{E}_{\rm rms}$ at time t for the scattering (blue) and focusing (red) experiments shown in figures 1 and 2, respectively. (b) Effect of ϵ on $\mathcal{E}_{\rm rms}$ for a set of scattering (blue, dots) and focusing (red, squares) experiments.

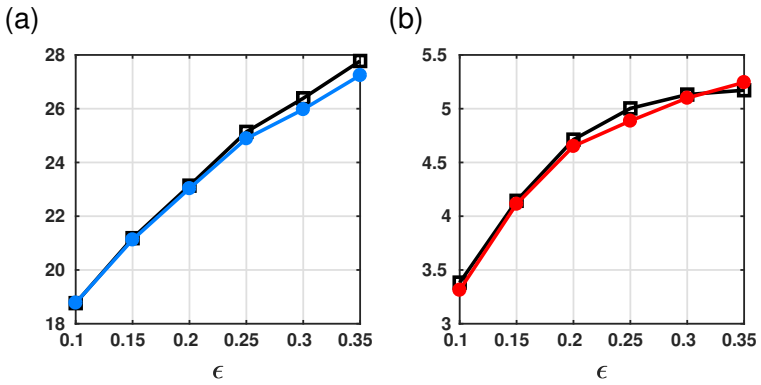

FIGURE 4. (a) Effect of ϵ on effective scattering angle θ_e (degrees) and comparison between amplitude equation (22) (blue, dots) and fully nonlinear equations (1) (black, squares) for scattering experiments. (b) Effect of ϵ on amplification and comparison between amplitude equation (red, dots) and fully nonlinear equations (black, squares) for focusing experiments. (See text for definitions of θ_e and amplification.)

We quantify the scattering of wave energy in spectral space, observed in figure 1(c) and 1(e) by using an effective scattering angle, θ_e, defined as:

$$\theta_e = \left(\int_R \theta^2(\boldsymbol{k}) |\hat{\eta}(\boldsymbol{k})| \, d\boldsymbol{k} \Big/ \int_R |\hat{\eta}(\boldsymbol{k})| \, d\boldsymbol{k} \right)^{1/2} \tag{26}$$

which is the square root of the normalized second moment of $|\hat{\eta}|$ weighted by its position θ in spectral space, where $\theta(\boldsymbol{k}) = \arctan(k_y/k_x)$. The moment is computed over the region R, which we take as the spectral ring $0.95 \leq k \leq 1.05$ and is shown in degrees in 4(a) as a function of ϵ, comparing the amplitude model (blue, dots) with the fully nonlinear equations (black, squares). The angle θ_e is a bulk measure for the angular spread of energy in spectral space, in which a larger angle indicates increased scattering. Observe that for all values of ϵ shown in figure 4(a), the measures of θ_e in the amplitude and fully nonlinear equations agree strongly.

For the focusing experiments, a natural quantity of interest is the amplitude maximum obtained at the focal point after equilibration. Figure 4(b) compares the maximum amplification obtained versus ϵ for the amplitude (red, dots) and fully nonlinear equations (black, squares). The amplification is computed as the average value of η/a for the points above the 75th percentile of the set

of positive points that lie within a 0.5λ radius of the focal point. The average was computed at the times when the focal point maximum reaches a peak value and was then time averaged over the last 10 peaks. There is again excellent agreement between the amplitude and fully nonlinear equations over the full range of ϵ shown.

We also observed strong agreement between the models for various other statistical quantities, such as the kurtosis of η (figure not shown). We therefore conclude that from a practical point of view, wave statistics are very well predicted by the amplitude equation even for relatively large topographies, for ϵ up to 0.35. Consequently, the new model would be very useful in obtaining wave statistics based on a large ensemble of simulations, a process that can be very expensive if attempted with the full set of equations.

4. Discussion

In this paper we introduced a new amplitude equation that captures the effect of small but spatially arbitrary bottom topography on monochromatic small amplitude surface gravity waves. Notably, the model does not require a spatial scale separation between the waves and the topography, nor restricts the wave field to a few wave modes, as has been the case with several previous popular models. The amplitude equation, being a single equation model, is an ideal simple asymptotic model for various applications. The fast wave oscillations are filtered out in the amplitude equation, thus allowing larger time steps to capture the slow modulation of the wave field. This results in considerable savings in the time required for numerical integration.

An important achievement of this paper is the demonstration that the amplitude equation in its regime of operation agrees very well with the fully nonlinear water wave equations, as was shown by our numerical simulations. Consequently, one may use the amplitude equation for various small amplitude wave-topography interaction problems, where the full set of equations have been used in the past. For instance, Elandt *et al.* (2014) integrated the full set of nonlinear equations to design specific topography to focus a monochromatic wave field. As seen in our simulation results presented in §3, the procedure can be carried out inexpensively by integrating the amplitude equation. The amplitude equation can be particularly useful when a large number of simulations are needed, especially from an engineering point of view, to optimize wave focusing topographies, for example.

As already pointed out before, the amplitude equation can be integrated with time steps $O(1/\epsilon)$ larger than that used to integrate the linear equations, the latter being required to track fast wave oscillations to obtain an accurate solution. Since our simulations show that the amplitude equation can substitute the full set of equations in the small amplitude regime, it is natural to ask – how fast can the amplitude equation be integrated, compared to the full set of equations (1)? To compare the speed up obtained by using the amplitude equation, we checked the time taken for both models to attain the scattered wave field shown in figure 1. We chose the scattering experiment for this test rather than the focusing experiment due to the wider spectral distribution of energy in the wave modes in the former case. The base solution was a highly accurate solution of (1) obtained using HOSM with M=4. We then used the amplitude equation and (1) using HOSM with M=3 to generate solutions for the speed test. Note that M=3 is the minimal order at which the effects of higher order resonances and nonlinear interactions appear in the numerical solution of (1). In this sense, the M=3 solution of (1) using HOSM serves as the least expensive nonlinear solution, which was also numerically converged – we found that the deviation of this solution from M=4 solution was minimal, similar to that seen in previous investigations (see for example tables 1-3 in Liu & Yue 1998 and their discussion). Within this set up, the amplitude equation and HOSM with M=3 were

integrated with the largest time steps possible so that $\mathcal{E}_{\text{rms}}$ computed for both of these approximate solutions with respect to the base solution was kept less than 20% at all times (the simulations were performed with two Intel(R) IvyBridge 3.00 GHz CPUs). For $\epsilon = 0.15$, the amplitude equation was seen to integrate 96.5 times faster than (1) integrated using HOSM with M=3. In addition to the speed up obtained due to removal of fast oscillations, the amplitude equation, being a single equation model, can be integrated in shorter time than the full set of equations integrated using HOSM which require time stepping of multiple variables.

Amplitude equation models for nonlinear surface wave-wave interactions have been extremely popular due to their inherent simplicity and ease of numerical integration (see for example Craik, 1985, Ablowitz, 2011 and references therein). Furthermore, amplitude equations have a significant advantage over more complex models when multiple realizations of the solution are needed to calculate various wave statistics – similar to the variables presented in figure 4. It is the lack of such models for wave-topography interactions that motivated this work. Given the simplicity and ease of numerical integration, we hope that this new model will benefit a wide scientific community in future.

Acknowledgments

We thank anonymous reviewers for constructive criticisms and suggestions.

JT is a postdoctoral research fellow hosted jointly by the Woods Hole Oceanographic Institution and Dalhousie University. RY is a NSF postdoctoral research fellow supported by the NSF award AGS-1624203.

Appendix A. Mathematical construction of bottom topography

The bottom topography used for numerical experiments discussed in §3 are shown in figure 5. The top row shows the three dimensional depiction of ζ for the scattering and focusing experiments while the bottom row shows the corresponding top views.

For the scattering experiments, the bottom topography ζ, shown in figures 5(a) and 5(c) was generated from a Gaussian random field on a torus (for double periodicity) with correlation length λ. ζ was made to have zero mean and was scaled so that its maximum height was ϵ.

For wave focusing experiments, we constructed a "concave mirror" topography following the procedure discussed in Elandt *et al.* (2014). We now derive the appropriate mathematical expression for the topography used in the numerical experiments.

Consider a wave with wavenumber $\boldsymbol{k}_1$, pointing in the positive x direction, interacting with a topography and thus resulting in the formation of a new wave with wavenumber $\boldsymbol{k}_2$. Since both waves should have same wavenumber magnitude to satisfy the resonance condition, we have $k_1 = k_2$, which can be used to write $\boldsymbol{k}_2 = (-k_1 \cos\vartheta, -k_1 \sin\vartheta)$, where $\vartheta = \tan^{-1}(y/x)$, for an arbitrary point (x, y). The topographic wavenumber, $\boldsymbol{k}_b$, is then given by their difference

$$\boldsymbol{k}_b = \boldsymbol{k}_2 - \boldsymbol{k}_1 = (-k_1(1 + \cos\vartheta), -k_1 \sin\vartheta) \tag{27}$$

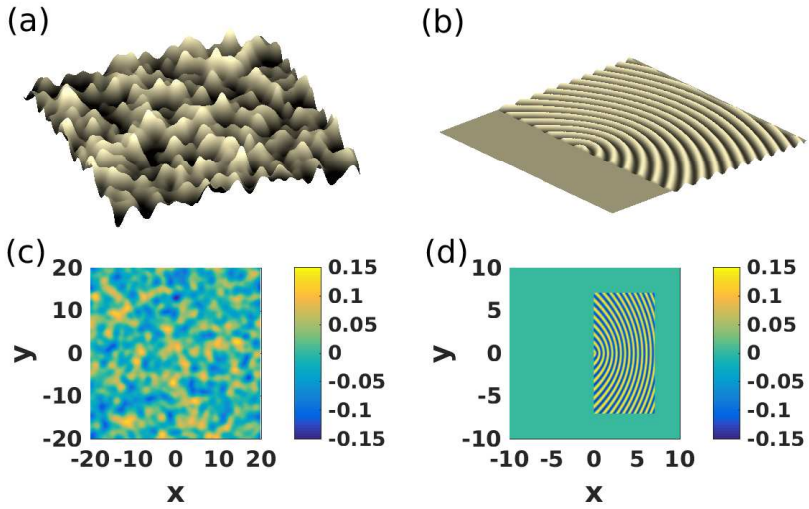

FIGURE 5. Topographic field ζ used for the scattering experiments shown in a three dimensional depiction (a) and from directly overhead (c). The colors shown in (c) are for the case with $\epsilon = 0.15$, corresponding to that used in figure 1. The random topography stretches across the entire domain. Topographic field for the focusing experiments with $\epsilon = 0.15$ are shown in (b) and (d) corresponding to that used in figure 2. ζ was computed using equation (31) in the patch shown and is zero outside the patch. Only a subdomain is shown with the full domain stretching from -20 to 20 in both x and y. The coordinates x and y are nondimensionalized by λ.

To obtain the topographic field $\zeta(x, y)$ from $\boldsymbol{k}_b$, we first define the vector field $\boldsymbol{n}_b(x, y)$ to be perpendicular to and of equal magnitude as $\boldsymbol{k}_b(x, y)$, where

$$\begin{aligned} \boldsymbol{n}_b &= k_1 \left(\sin\vartheta, -(1+\cos\theta)\right) \\ &= k_1 \left(\frac{y}{\sqrt{x^2+y^2}}, -\left(1 + \frac{x}{\sqrt{x^2+y^2}}\right)\right) \end{aligned} \tag{28}$$

It is easily checked that $\boldsymbol{n}_b$ is divergence free, i.e. $\partial n_{bx}/\partial x + \partial n_{by}/\partial y = 0$. Therefore we can define a scalar field $\Psi(x, y)$ such that $\boldsymbol{n}_b = (\partial\Psi/\partial y, -\partial\Psi/\partial x)$. Straightforward integration of (28) gives

$$\Psi(x, y) = k_1 \left(x + \sqrt{x^2+y^2}\right) \tag{29}$$

Note that contours of ζ and Ψ coincide. Additionally, for any point (x, y), one can follow the contours of Ψ and find the corresponding point on the x-axis. Mathematically, for any point (x, y), $x \geq 0$, there is a unique point $(X, 0)$, $X \geq 0$ such that $\Psi(x, y) = \Psi(X, 0)$ (we restrict our topography to the right half of the domain). Then, from (29) we get

$$X = \frac{1}{2}\left(x + \sqrt{x^2+y^2}\right) \tag{30}$$

We therefore construct a rippled topography by setting $\zeta = -\sin(k_{bx}X)$, where $k_{bx} = -2k_1$ is the restriction of the x component of (27) on the $x-$axis. Finally, using (30) in the above expression for ζ, we get the expression for the topography used in the numerical experiments discussed in §3,

$$\zeta(x, y) = \sin\left\{k_1 \left(x + \sqrt{x^2+y^2}\right)\right\} \tag{31}$$

We note that our choice of the sine function for the topography equation (31) is arbitrary, as one could have used another oscillatory function such as cosine instead.

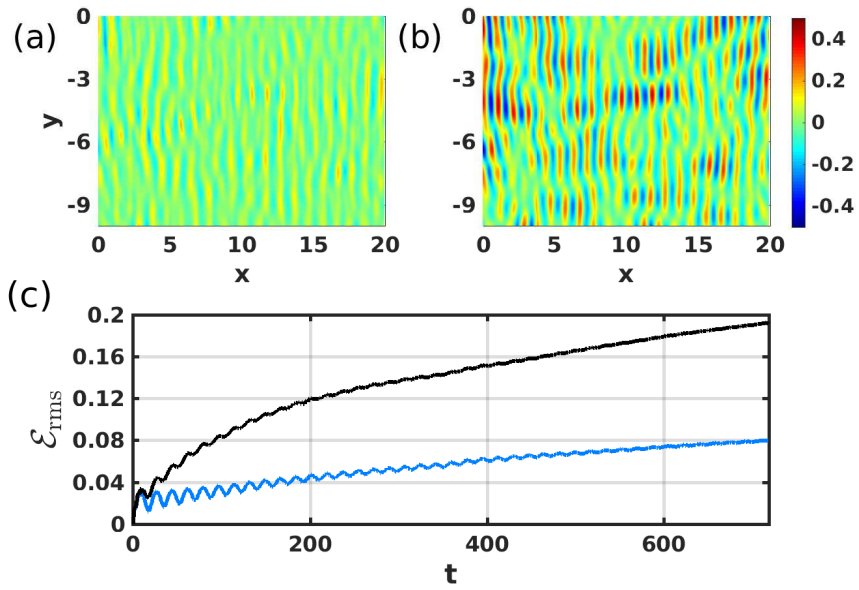

FIGURE 6. Top row: difference of η computed with (a) improved amplitude model (22) and HOSM and (b) amplitude model (17) and HOSM, for the scattering experiment in figure 1. The panels shown here correspond to the same time and spatial location as those shown in figure 1 (b),(d). Notice that the improved model has relatively less pointwise errors. Bottom: root-mean-square error, $\mathcal{E}_{\text{rms}}$, versus time for the scattering experiment in figure 1 when computed with the improved amplitude model (22) (blue) and amplitude model (17) (black). Observe that the improved model accumulates less error over time compared to the original model.

APPENDIX B. DISPERSIVE CORRECTION OF THE AMPLITUDE EQUATION

Here we present an example to demonstrate the improvement achieved by modifying the dispersive characteristics of the first amplitude equation (17) to obtain our preferred reduced model (22). For the scattering experiment described in §3.1, we compared both the amplitude equations (17) and (22) against the full set of equations (1) simulated using HOSM. Figure 6 shows this comparison for the case $\epsilon = 0.15$, corresponding to the case presented in figure 1. The top panel of figure 6 shows the pointwise error between the amplitude models and full set of equations, while the bottom panel shows the time series of rms error. It is clear that the improved model performs relatively better, with less pointwise and rms error at any given time during the simulation. This improved performance of the model (22), based on numerical experiments, justifies the modification of the dispersive characteristics of the original amplitude equation (17) to obtain (22).

REFERENCES

ABLOWITZ, M.J. 2011 *Nonlinear Dispersive Waves-Asymptotic Analysis and Solitons*. Cambridge University Press, Cambridge.

ALAM, M.-R., LIU, Y. & YUE, D. K. P. 2009 Bragg resonance of waves in a two-layer fluid propagating over bottom ripples. part 2. numerical simulation. *J. Fluid Mech.* **624**, 225–253.

ALAM, M.-R., LIU, Y. & YUE, D. K. P. 2010 Oblique sub- and super-harmonic bragg resonance of surface waves by bottom ripples. *J. Fluid Mech.* **643**, 437–447.

Battjes, J. A. 1988 Surf-zone dynamics. *Ann. Rev. Fluid mech.* **20**, 257–291.

Berkhoff, J. C. W. 1973 Computation of combined refraction-diffraction. *Proc. 13th Intl Conf. on Coastal Engng, July 1972, Vancouver, Canada, ASCE* pp. 471–490.

Blondeaux, P. 1990 Sand ripples under sea waves. part 1: Ripple formation. *J. Fluid Mech.* **218**, 1–17.

Chamberlain, P.G. & Porter, D. 1995 The modified mild-slope equation. *J. Fluid Mech.* **291**, 393–407.

Couston, L.A., Jalali, M.A. & Alam, M.-R. 2017 Shore protection by oblique seabed bars. *J. Fluid Mech.* **815**, 481–510.

Craik, A.D.D. 1985 *Wave Interactions and Fluid Flows*. Cambridge University Press, Cambridge.

Davies, A. G. 1982 The reflection of wave energy by undulations on the seabed. *Dyn. Atmos. Oceans* **6**, 207–232.

Dolan, T. J. & Dean, R.G. 1985 Multiple longshore sand bars in the upper chesapeake bay. *Estuar., Coast. Shelf Sci.* **21**, 727–743.

Dommermuth, D. G. & Yue, D. K. P. 1987 A high-order spectral method for the study of nonlinear gravity waves. *J. Fluid Mech.* **184**, 267–288.

Dysthe, K. B. 1979 Note on a modification to the nonlinear Schrödinger equation for application to deep water waves. *Proc. R. Soc. London Ser. A* **369**, 105–114.

Elandt, R. B., Shakeri, M. & Alam, M.-R. 2014 Surface gravity-wave lensing. *Phys. Rev. E* **89**, 023012.

Elgar, S., Raubenheimer, B. & Herbers, T.H.C. 2003 Bragg reflection of ocean waves from sandbars. *Geophys. Res. Lett.* **30**, 16:1–4.

Evans, D. V. 1981 Power from water waves. *Ann. Rev. Fluid mech.* **13**, 157–187.

Griffiths, L.S. & Porter, R. 2012 Focusing of surface waves by variable bathymetry. *Appl. Ocean Res.* **34**, 150–163.

Hancock, M. J., Landry, B. J. & Mei, C. C. 2008 Sandbar formation under surface waves: theory and experiments. *J. Geophys. Res.* **113**, C07022.

Heathershaw, A. D. 1982 Seabed-wave resonance and sand bar growth. *Nature* **296**, 343–345.

Hinch, E. J. 1991 *Perturbation Methods*. Cambridge University Press, Cambridge.

Hu, X & Chan, C.T. 2005 Refraction of water waves by periodic cylinder arrays. *Phys. Rev. Lett.* **95**, 154501.

Keller, J.B. 1958 Surface waves on water of non-uniform depth. *J. Fluid Mech.* **4**, 607–614.

Kirby, J. T. 1986 A general wave equation for waves over rippled beds. *J. Fluid Mech.* **162**, 171–186.

Liu, Y. & Yue, D. K. P. 1998 On generalized bragg scattering of surface waves by bottom ripples. *J. Fluid Mech.* **356**, 297–326.

Mandlier, P.G. 2013 Field observations of wave refraction and propagation pathways on coral reef platforms. *Earth Surf. Process. Landforms* **38**, 913–925.

Mei, C. C. 1983 *Applied Dynamics of Ocean Surface Waves*. Wiley-Interscience.

Mei, C. C. 1985 Resonant reflection of surface water waves by periodic sandbars. *J. Fluid Mech.* **152**, 315–335.

Mei, C. C. 2012 Hydrodynamic principles of wave power extraction. *Phil. Trans. R. Soc. A.* **370**, 208–234.

Miles, J.W. & Chamberlain, P.G. 1998 Topographical scattering of gravity waves. *J. Fluid Mech.* **361**, 175–188.

Munk, W.H. & Traylor, M.A. 1947 Refraction of ocean waves: A process linking underwater topography to beach erosion. *The Journal of Geology* **55**, 1–26.

Peregrine, D. H. 1983 Breaking waves on beaches. *Ann. Rev. Fluid mech.* **15**, 149–178.

Roberts, A. J. 1985 An introduction to the technique of reconstitution. *SIAM J. Math. Anal.* **16**, 1243–1257.

Smith, R. & Sprinks, T. 1975 Scattering of surface waves by a conical island. *J. Fluid Mech.* **72**, 373–384.

Stamnes, J.J., Lovhaugen, O., Spjelkavik, B., Mei, C.C., Lo, E. & Yue, D.K.P. 1983 Nonlinear focusing of surface waves by a lens - theory and experiment. *J. Fluid Mech.* **135**, 71–94.

Thomas, J. 2016 Resonant fast-slow interactions and breakdown of quasi-geostrophy in rotating shallow water. *J. Fluid Mech.* **788**, 492–520.

Thomas, J. 2017 New model for acoustic waves propagating through a vortical flow. *J. Fluid Mech.* **823**, 658–674.

Thomas, J., Smith, K.S. & Bühler, O. 2017 Near-inertial wave dispersion by geostrophic flows. *J. Fluid Mech.* **817**, 406–438.

Trulsen, K. & Dysthe, K. B. 1996 A modified nonlinear Schrödinger equation for broader bandwidth gravity waves on deep water. *Wave Motion* **24**, 281–289.

Wagner, G. L., Ferrando, G. & Young, W. R. 2017 An asymptotic model for the propagation of oceanic internal tides through quasi-geostrophic flow. *J. Fluid Mech.* **828**, 779–811.

Wagner, G. L. & Young, W. R. 2016 A three-component model for the coupled evolution of near-inertial waves, quasi-geostrophic flow and the near-inertial second harmonic. *J. Fluid Mech.* **802**, 806–837.

West, B. J., Brueckner, K. A., Janda, R. S., Milder, D. M. & Milton, R. L. 1987 A new numerical method for surface hydrodynamics. *J. Geophys. Res.* **92**, 11803–11824.

Yu, J. & Mei, C. C. 2000*a* Do longshore bars shelter the shore? *J. Fluid Mech.* **404**, 251–268.

Yu, J. & Mei, C. C. 2000*b* Formation of sand bars under surface waves. *J. Fluid Mech.* **416**, 315–348.